ADVANCED FUNCTIONAL MATERIALS
www.afm-journal.de

Modulation on Surface Termination Groups to Optimize the Adsorption Energy and Work Function of Nb_2CT_x for Enhanced Hydrogen Storage in Magnesium Hydride

Tao Zhong, Tian Xu, Liuting Zhang, Li Wang, Fuying Wu, and Xuebin Yu**

Exploring high-performance catalysts for hydrogen storage in magnesium hydride (MgH_2) is crucial but still a challenge. Herein, Nb_2CT_x with controllable surface termination groups is developed as an efficient catalyst and the bifunctional modulation (adsorption energy and work function) of different surface termination groups (–F, –O, –OH, or defects) is explored. First, compared to –F and –O, the introduction of –OH on the surface or the direct removal of functional groups both leads to a significant increase in the adsorption of H by Nb_2CT_x. Second, compared to the surface bare, –OH-rich Nb_2CT_x has a lower work function, making it easier for hydrogen to enter Mg/MgH_2 from the Nb_2CT_x surface or escape from the Mg/MgH_2 surface into the Nb_2CT_x, thus facilitating the hydrogen ad/desorption properties of MgH_2, i.e., the rate-determining step (RDS) shifts from penetration to diffusion. The Nb_2CT_x-KOH-catalyzed MgH_2 with optimal surface termination groups, therefore exhibits a release of 6.56 wt.% H_2 in 5 min at 250 °C, and 6.46 wt.% H_2 uptake within 5 min at 150 °C. The dehydrogenation and hydrogen uptake activation energies show 49.5% and 60.1% enhancements over pristine MgH_2. In addition, a storage capacity of 5.51 wt.% is maintained after 50 dehydrogenation/hydrogenation cycles.

1. Introduction

Hydrogen has been recognized as a potential clean energy carrier for the development of carbon-neutral systems due to its natural abundance, cleanliness, and high energy density, which is important for achieving the global transition to a sustainable energy economy.[1] Unfortunately, the lack of a suitable hydrogen storage solution constrains the large-scale utilization of hydrogen.[2] Reversible storage of hydrogen in metal hydrides offers inherent advantages of high safety, low cost, and excellent hydrogen storage capacity.[3] Among a wide range of solid-state hydrogen storage materials, MgH_2 is particularly favored for its excellent reversibility with weight and volumetric hydrogen densities of 7.6 wt.% and 110 kg m^{-3}, respectively.[4] However, the sluggish kinetics and ultra-high dehydrogenation barrier make the current hydrogen storage performance of MgH_2 inadequate for practical applications.[5]

To improve its hydrogen storage performance, alloying,[6] nanocrystallization,[7] compositing,[8] and catalytic doping have been proposed by researchers.[9] In particular, various catalysts have been intensively investigated because they can improve the kinetics of hydrogen adsorption and desorption.[10] MXenes as a class of highly interesting 2D materials consist of transition metal carbides or nitrides.[11] The general chemical formula of MXenes is $M_{n+1}X_nT_x$, where M denotes an early transition metal (Ti, Mo, Nb, or V), X denotes a carbide (C) or a nitride (N), and T_x is the surface terminus (–O, –OH, –F, or –Cl).[12] They can be obtained by etching an A-element layer from the native $M_{n+1}AX_n$ phase (A = Al, Ga, etc.).[13] MXene offers unique interlayer space, high specific surface area, tunable composition, as well as abundant and controllable surface terminations.[14] Due to its 2D layered structure, MXene exhibits high surface area properties, which leads to the uniform dispersion of its nanosheets on Mg/MgH_2.[15] The Transition metals in the MXene lattice are regarded as effective centers of catalytic activity that can enhance the rate of de/hydrogenation.[16] Remarkably, the etching process results in the formation of different surface termination groups (–O, –OH, –F, or –Cl) on MXene,[17] and it has been proposed that the properties of MXene can be manipulated by adjusting the ratio of surface termination groups.[18] Lv et al.[19] investigated the catalytic ability of several bare and –OH-terminated MXenes for electrochemical nitrogen reduction reactions (NRR). It was found that the H atoms in –OH can be trapped by the intermediates and participate in the NRR process. Cai et al.[20] functionalized Ti_3C_2 MXene by introducing terminal oxygen groups and found that the in situ converted surface hydroxyl groups were identified as a new active site for nitrate

T. Zhong, L. Zhang, L. Wang, F. Wu
School of Energy and Power
Instrumental Analysis Center
Jiangsu University of Science and Technology
Zhenjiang 212003, China
E-mail: zhanglt89@just.edu.cn
T. Xu, X. Yu
Department of Materials Science
Fudan University
Shanghai 200433, China
E-mail: yuxuebin@fudan.edu.cn

The ORCID identification number(s) for the author(s) of this article can be found under https://doi.org/10.1002/adfm.202418230

DOI: 10.1002/adfm.202418230

reduction. Huang et al.[21] regulated the surface termination groups of Nb_2CT_x by alkali and annealing treatments, verified that different surface termination groups could effectively regulate the work functions of MXene. Whereas in the field of Mg-based hydrogen storage, Gao et al.[22] introduced 2D $Ti_3C_2T_x$ MXenes exposing different active facet to MgH_2, revealed that the edge facet with smaller work function (5.64 eV) possesses stronger catalytic activity compared to the basal facet (5.86 eV). Huang et al.[23] showed theoretically that H atoms can recombine into H_2 at the interface of –O/–OH modified Ti_2C and MgH_2 heterostructures. Kim et al.[24] experimentally developed a –Cl end-modified Ti_2C with a strategy that improved catalysis by forming an intimate interface between magnesium and MXene to facilitate charge transfer. Zhou et al.[25] used Nb_2CT_x as an example to show that a proper T_x defect density is central to the effective catalytic activity of Nb_2CT_x. When the defect density is too high, Nb strongly interacts with dissociated hydrogen, leading to a deterioration of Mg kinetic properties.

However, systematic experimental studies on the effect of different surface termination groups on the catalytic activity of MXene are still lacking. Here in this work, we subjected Nb2CTx to alkali treatment and annealing in different atmospheres to modulate its surface termination groups and explore the corresponding catalytic activity, which provides a fundamental exploration for the application of other MXenes in Mg-based hydrogen storage. After 12 h of KOH treatment, the –F of pristine Nb_2CT_x can be replaced by –OH. After annealing under Ar atmosphere, a part of –OH was transformed into –O groups. In addition, heat treatment under H_2 atmosphere can create defects on the surface of Nb_2CT_x. Unexpectedly, the –OH richen Nb_2CT_x-KOH showed optimal catalytic performance for MgH_2, dehydrogenating 6.56 wt.% in 5 min at 250 °C and adsorbing 5.75 wt.% of H_2 in 15 min at 75 °C. DFT calculations and analyses of the rate-determining step (RDS) show that the hydrophilic properties of Nb_2CT_x can be controlled by changing the surface termination groups of Nb_2CT_x. The hydrogen affinity of pure Nb_2C and –OH is stronger compared to –F and –O. Work function and PDOS analyses show a lower work function of 2.24 eV for the –OH model compared to 4.45 eV for the pure Nb_2C, suggesting that electrons are more likely to escape from the –OH surface into the hydrogen, thus facilitating reduction. The d bond center calculated from the PDOS of the Nb 4d orbital is also closer to the Fermi level in the –OH model, suggesting that the d electrons are more likely to transition to the conduction band to catalyze the hydrogen storage reaction.

2. Results and Discussion

Figure 1a shows a schematic diagram of the 2D Nb_2CT_x synthesis process. The Al layer of MAX phase Nb_2AlC was removed by a 39% HF solution. The terminal –F group in pristine Nb_2CT_x was replaced with –OH by treating with KOH solution. The KOH-treated Nb2CTx was then annealed under argon for 12 h to convert –OH to –O. The etched and KOH-treated Nb_2CT_x were simultaneously annealed under H_2 to remove surface termination groups. In this paper, the etched, alkali-treated, and heat-treated samples were denoted as Nb_2CT_x-pristine, Nb_2CT_x-KOH, Nb_2CT_x-H_2, Nb_2CT_x-KOH-Ar, and Nb_2CT_x-KOH-H_2, respectively. Figure 1b shows the SEM images of all the samples. The pristine Nb_2CT_x (Figure 1bII) showed a relaxed accordion-like structure, suggesting that the aluminum layer had been successfully removed. Furthermore, all morphologies remained well intact after KOH as well as argon and hydrogen annealing treatments, suggesting that the KOH and the annealing treatments did not damage the Nb_2CT_x. Figures S1–S3 (Supporting Information) show the EDS spectra of Nb_2AlC, Nb_2CT_x-pristine, and Nb_2CT_x-KOH, respectively. It can be seen that etching resulted in the removal of the Al layer, and the removal of the –F group after KOH treatment. In the XRD patterns (Figure 1c–e), the main (006) diffraction peak (at ≈38° 2θ) of Nb_2AlC disappeared compared to that of Nb_2CT_x-pristine, suggesting that the Al element was successfully etched after HF treatment. Following KOH treatment, the (002) peak shifted to a smaller angle, indicating the interlayer spacing was enlarged and the specific surface area was increased.[26] On the contrary, the (002) peak shifted to a higher angle after annealing, demonstrating the removal of –OH and the decrease of interlayer spacing.[27] It is noteworthy that the least interlayer spacing was found in Nb_2CT_x-KOH-H_2. The specific layer spacing for each sample calculated from the Bragg equation is shown in Table S1. In addition, after KOH and annealing treatment, the niobium oxides had no obvious diffraction peaks.

In order to explore the effects of KOH and annealing treatment on the surface termination groups of Nb_2CT_x, XPS tests were performed. Figure S4, (Supporting Information) illustrates the full-scan spectra of all the samples, in which Nb_2CT_x consists mainly of Nb, C, O, and F. **Figure 2** shows the fine scanning spectra of Nb, C, O, and F for all samples. Among them, there are six peaks in the Nb 3d region near 210.19, 207.64, 206.95, 208.42, 205.07, and 204.06 eV,[28] corresponding to Nb_2O_5 3d3/2, NbC_xO_y 3d3/2, Nb_2O_5 3d5/2, Nb–C 3d3/2, NbC_xO_y 3d5/2, and Nb–C 3d5/2.[29] The peak fitting results are detailed in Table S3. NbC_xO_y 3d3/2 and NbC_xO_y 3d5/2 correspond to the surface termination groups (–O and –OH). As can be seen from Figure 2, the peak intensity of NbC_xO_y in the Nb 3d region decreases after heat treatment under H_2 atmosphere and increases with KOH treatment. The content of –O in Nb_2CT_x decreased after heat treatment under H_2 atmosphere. The content of –OH in Nb_2CT_x increased after treatment with KOH (Table S3). This trend is also consistent with the results of O 1s and F 1s, i.e., the content of –O decreased from 25% to 20% and the content of –F decreased from 50% to 25% after heat treatment under H_2 atmosphere. It is noteworthy that the peak belonging to C-Nb-T_x is found near 282.51 eV for C 1s, which shows that the content of C-Nb-T_x decreases from 100% to 70% after hydrogen reduction, thus creating some defects. Whereas the content of –OH increases from 20% to 50% and the content of –F decreases from 50% to 0% after KOH treatment. The results manifest that hydrogen reduction allowed surface termination groups to be partially removed while alkali treatment results in the substitution of the –F group by the –OH group. The peak intensity of NbC_xO_y in the Nb 3d region decreased with annealing under Ar compared to Nb_2CT_x-KOH. The result was shown in O 1s, The content of –OH in Nb_2CT_x decreased from 50% to 35%, while the –O content increased from 50% to 65% (Table S3). This may be due to the high-temperature removal of –OH or the conversion of –OH to –O.[24] Similarly in C 1s, the peak belonging to C-Nb-T_x ≈282.17 e.V further decreases from 70% to 45% for Nb_2CTx reduced by KOH treatment

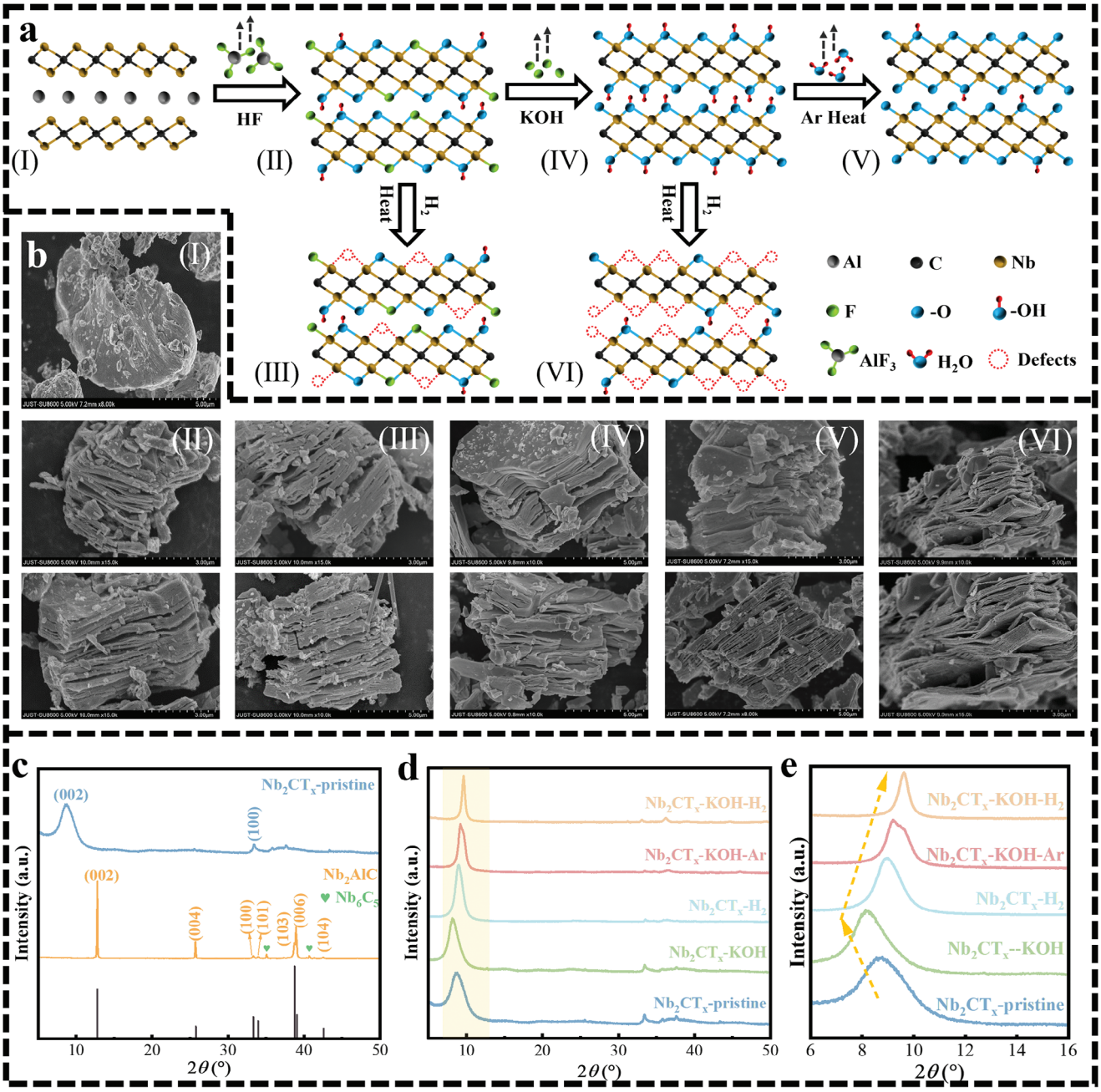

Figure 1. a) Schematic diagram for the synthesis of Nb_2CT_x MXene; b) SEM, c–e) XRD patterns of Nb_2AlC, Nb_2CT_x-pristine, Nb_2CT_x-KOH, Nb_2CT_x-H_2, Nb_2CT_x-KOH-Ar, and Nb_2CT_x -KOH-H_2.

followed by hydrogen reduction compared to direct hydrogen reduction. This may be attributed to the fact that –OH is more easily removed under hydrogen as compared to –F. Finally, on the basis of the fitting results for Nb 3d, O 1s, F 1s, and C 1s, the chemical formulae were established as $Nb_2CO_{0.6}OH_{0.4}F_{1.0}$ (Nb_2CT_x-pristine), $Nb_2CO_{0.5}OH_{0.4}F_{0.5}Defect_{0.6}$ (Nb_2CT_x-H_2), $Nb_2CO_{1.0}OH_{1.0}$ (Nb_2CT_x-KOH), $Nb_2CO_{1.3}OH_{0.7}$ (Nb_2CT_x-KOH-Ar), $Nb_2CO_{0.5}OH_{0.4}Defect_{1.1}$ (Nb_2CT_x-KOH-H_2).

Figure 3 shows the isothermal dehydrogenation kinetics of Nb_2CT_x-pristine, Nb_2CT_x-KOH, Nb_2CT_x-H_2, Nb_2CT_x-KOH-Ar, and Nb_2CT_x-KOH-H_2 at different temperatures and the corresponding activation energies were calculated according to the Arrhenius equation. All five samples exhibited superior dehydrogenation kinetics compared to milled-MgH_2 (Figure S9, Supporting Information). At 280 °C, all five composites were able to release all the hydrogen within 15 min. Notably, Nb_2CT_x-KOH and Nb_2CT_x-KOH-Ar showed further improvement in performance compared to pristine Nb_2CT_x, where Nb_2CT_x-KOH was even able to release 6.56 wt.% of hydrogen in just 5 min at a low temperature of 250 °C. On the contrary, the performance

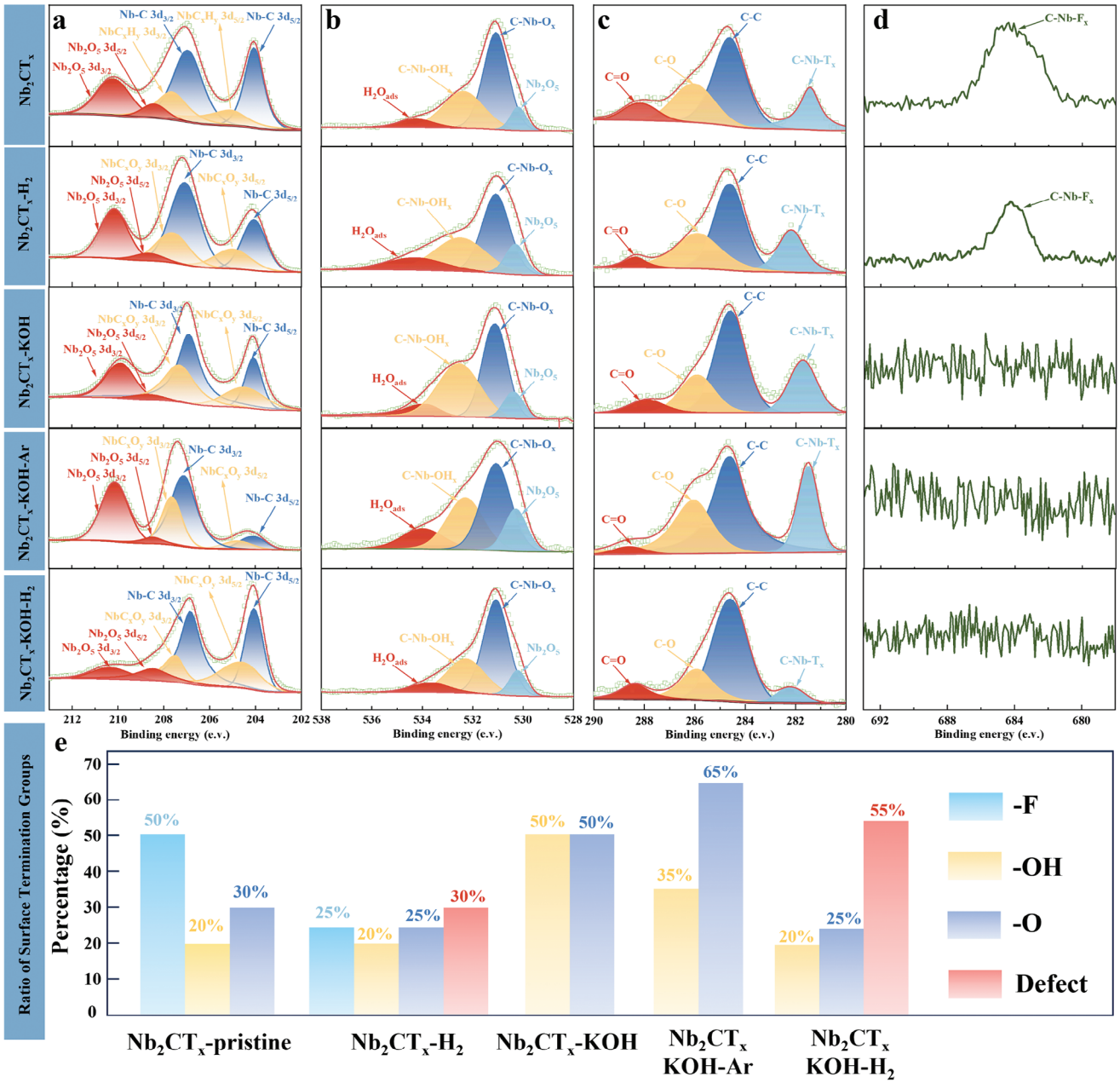

Figure 2. High resolution XPS spectra of a) Nb 3d; b) O 1s; c) C 1s; d) F 1s of Nb_2CT_x-pristine, Nb_2CT_x-H_2, Nb_2CT_x-KOH, Nb_2CT_x-KOH-Ar, and Nb_2CT_x-KOH-H_2. e) The ratio of surface termination groups.

of Nb_2CT_x-H_2 and Nb_2CT_x-KOH-H_2 instead decreased compared to pristine Nb_2CT_x, with Nb_2CT_x-KOH-H_2 having the worst dehydrogenation kinetics. Figure 3f illustrates the dehydrogenation curves of the five samples at 250 °C, showing the same results. The non-isothermal desorption curves and differential calculations (Figures S6 and S7, Supporting Information) also exhibit the same trends, with Nb_2CT_x-KOH/MgH_2 reaching the maximum dehydrogenation rate value at the lowest temperature. To further compare the difference in the dehydrogenation performance of the five composites, we calculated the normalized H_2 desorption capacity at 250 and 280 °C, which visually demonstrates the difference in the H_2 desorption ratio over time (Figure 3g). The Nb_2CT_x-KOH/MgH_2 released 100% H_2 within 5 min at both 250 and 280 °C, whereas the other samples needed much longer time to complete dehydrogenation. In particular, as much as 59% and 55% of the hydrogen was discharged at 250 °C for Nb_2CT_x-H_2 and Nb_2CT_x-KOH-H_2 in the time period of 10–30 min. To gain insight into the dehydrogenation kinetics of the samples, we calculated the activation energies for dehydrogenation of milled-MgH_2 and the five composites by the Arrhenius equation (Figure 3h; Figures S9e and S10, Supporting Information).[30] The calculated Nb_2CT_x-KOH possesses the

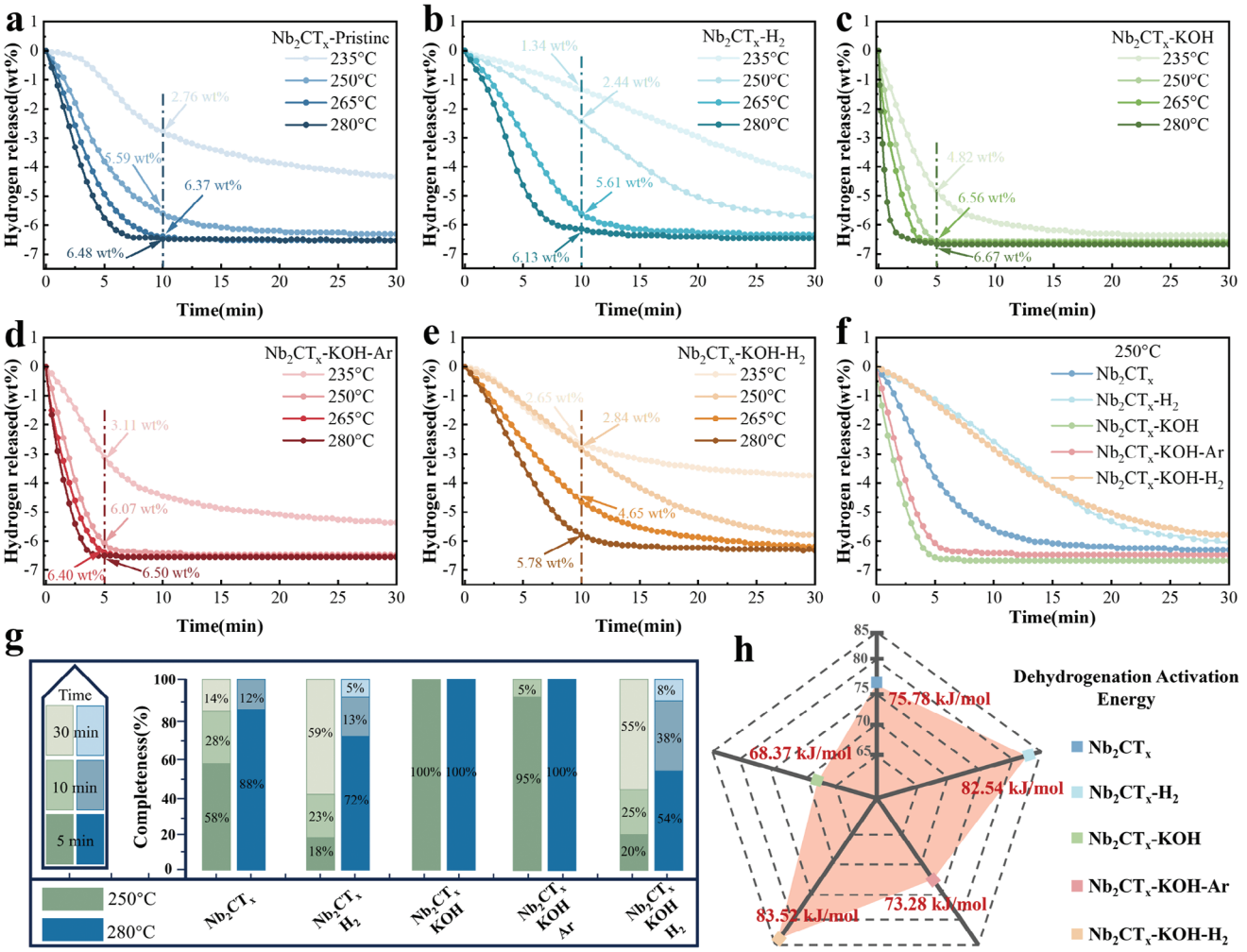

Figure 3. Desorption curves of a) Nb_2CT_x-pristine/MgH_2, b) Nb_2CT_x-H_2/MgH_2, c) Nb_2CT_x-KOH/MgH_2, d) Nb_2CT_x-KOH-Ar/MgH_2, e) Nb_2CT_x-KOH-H_2/MgH_2, and f) their comparisons at 250 °C in isothermal mode; g) Normalized H_2 release capacity of MgH_2 catalyzed by five MXene at 250 and 280 °C; h) Comparison of dehydrogenation activation energy of five composites.

lowest activation energy (68.37 kJ mol^{-1}), which is 49.5% lower compared to milled-MgH_2 (135.32 kJ mol^{-1}). All the results indicate the strength of catalytic activity in the order of Nb_2CT_x-KOH-H_2< Nb_2CT_x-H_2< Nb_2CT_x-pristine< Nb_2CT_x-KOH-Ar< Nb_2CT_x-KOH.

The hydrogenation rates of Nb_2CT_x-pristine, Nb_2CT_x-KOH, Nb_2CT_x-H_2, Nb_2CT_x-KOH-Ar, and Nb_2CT_x-KOH-H_2 are shown in **Figure** 4a–e. The results demonstrate that the kinetic performance of hydrogenation of all five composites is greatly improved compared to milled-MgH_2 (Figure S9b, Supporting Information). Among them, Nb_2CT_x-KOH has the most outstanding hydrogenation kinetic performance, which could adsorb 6.45 wt.% H_2 within 5 min at 150 °C and 6.39 wt.% H_2 within 30 min at 75 °C. Figure 4f demonstrates the hydrogenation profiles of the five samples at 125 °C, where within 5 min Nb_2CT_x-KOH, Nb_2CT_x-KOH-Ar, Nb_2CT_x-pristine, Nb_2CT_x-H_2 and Nb_2CT_x-KOH-H_2 could absorb 6.12, 5.35, 4.69, 3.94, and 2.85 wt.% of H_2, respectively, demonstrating the same order of catalytic activity strengths as for dehydrogenation reactions. The hydrogenation activation energies of milled-MgH_2 and the five composites were also calculated by the Arrhenius equation (Figure 4h; Figures S9f and S11, Supporting Information). Nb_2CT_x-KOH has the lowest hydrogenation activation energy (33.02 kJ mol^{-1}), which is 60.1% lower compared to milled-MgH_2 (82.76 kJ mol^{-1}), and 15.0% lower compared to the Nb_2CT_x-pristine (38.79 kJ mol^{-1}).

Combining the XPS fitting results and the hydrogen absorption and discharge performance tests, it can be concluded that Nb_2CT_x-KOH enriched with –OH surface groups has the most excellent catalytic activity, followed by Nb_2CT_x-KOH-Ar enriched with –O groups, both of which outperform the pristine Nb_2CT_x-pristine. However, the surface-rich defects of Nb_2CT_x-H_2 and Nb_2CT_x-KOH-H_2 exhibited poorer performance than the original Nb_2CT_x-pristine, with the more defect-rich Nb_2CT_x-KOH-H_2 performing worse than the less defect-rich Nb_2CT_x-H_2, which is consistent with the DFT calculations of Zhou et al.[25] Bare Nb_2C is prone to form strong Nb-H bonds with H, which makes the hydrogen dissociation state more stable than the initial state, which ultimately leads to difficulties in hydrogen diffusion.

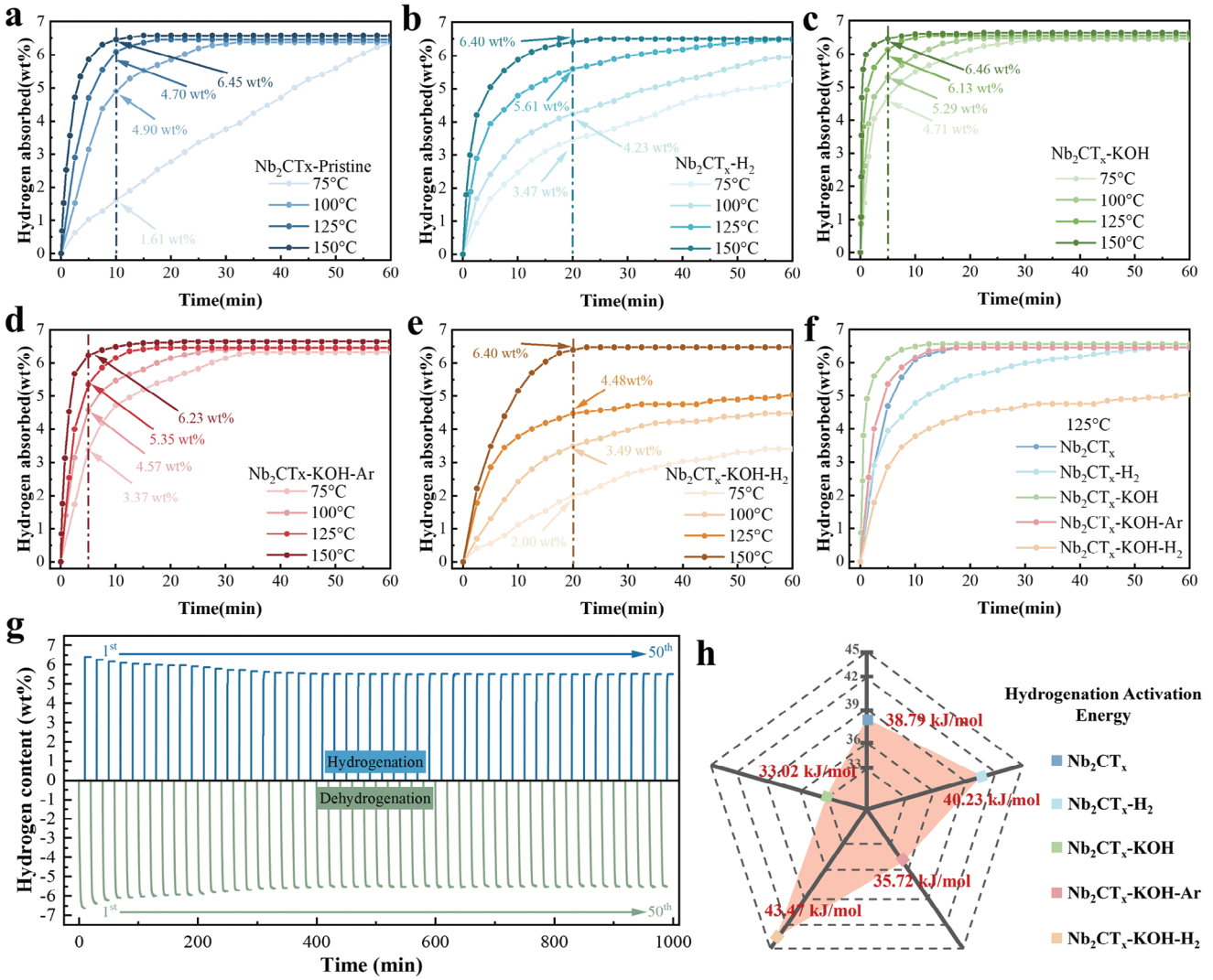

Figure 4. Absorption curves of a) Nb_2CT_x-pristine/MgH_2, b) Nb_2CT_x-H_2/MgH_2, c) Nb_2CT_x-KOH/MgH_2, d) Nb_2CT_x-KOH-Ar/MgH_2, e) Nb_2CT_x-KOH-H_2/MgH_2, and f) their comparisons at 125 °C in isothermal mode; g) Isothermal hydrogen de/absorption cycle curves of Nb_2CT_x-KOH/MgH_2 composites at 280 °C; h) Comparison of hydrogenation activation energy of five composites.

Consequently, the best adsorption and desorption performance of Nb_2CT_x-KOH/MgH_2 was subjected to 50 isothermal dehydrogenation/hydrogenation reactions at 280 °C, as shown in Figure 4g. The initial hydrogen storage capacity was 6.64 wt.%. In the first 25 cycles, the hydrogen storage capacity decreased to 5.51 wt.%. Nb_2CT_x-KOH/MgH_2 shows a stable dehydrogenation reaction, and the hydrogen storage capacity remained at 5.51 wt.% until the 50th cycle. The variation of dehydrogenation/hydrogenation kinetics over the course of the cycle is shown in Figure S12, (Supporting Information). Similar to the cycling capacity, the kinetic rate slowed down in the first 20 cycles, but remained stable thereafter. In addition, we compared the hydrogen uptake and discharge performance of Nb_2CT_x-KOH/MgH_2 at the 50th cycle with the first hydrogen uptake and discharge performance of Nb_2CT_x-KOH-H_2/MgH_2, the results show that the kinetic performance of Nb_2CT_x-KOH/MgH_2 in the 50th cycle was still superior to that of Nb_2CT_x-KOH-H_2/MgH_2, which means that Nb_2CT_x-KOH was not converted to Nb_2CT_x-KOH-H_2 during the cycling process.[31]

The catalytic mechanism of Nb_2CT_x on MgH_2 was systematically investigated in terms of RDS, XRD, TEM, XPS, and DFT calculation results. The isothermal de/hydrogenation curves of the five composites were fitted to the Chou model (Figure S14, Supporting Information), and the RDS of the de/hydrogenation reaction was derived to gain a deeper insight into the kinetic mechanism.[32] The de/hydrogenation of MgH_2 in the Chou model involves penetration and diffusion-determining steps, of which the diffusion model is the faster step in the hydrogen de/adsorption process. As shown in the dehydrogenation fits in Figure S14a–f, (Supporting Information) and hydrogenation fits in Figure S14g–i, (Supporting Information), Nb_2CT_x-KOH/MgH_2 both converted from the permeation model to the diffusion model at lower temperatures, followed by Nb_2CT_x-KOH-Ar/MgH_2. While Nb_2CT_x-pristine/MgH_2,

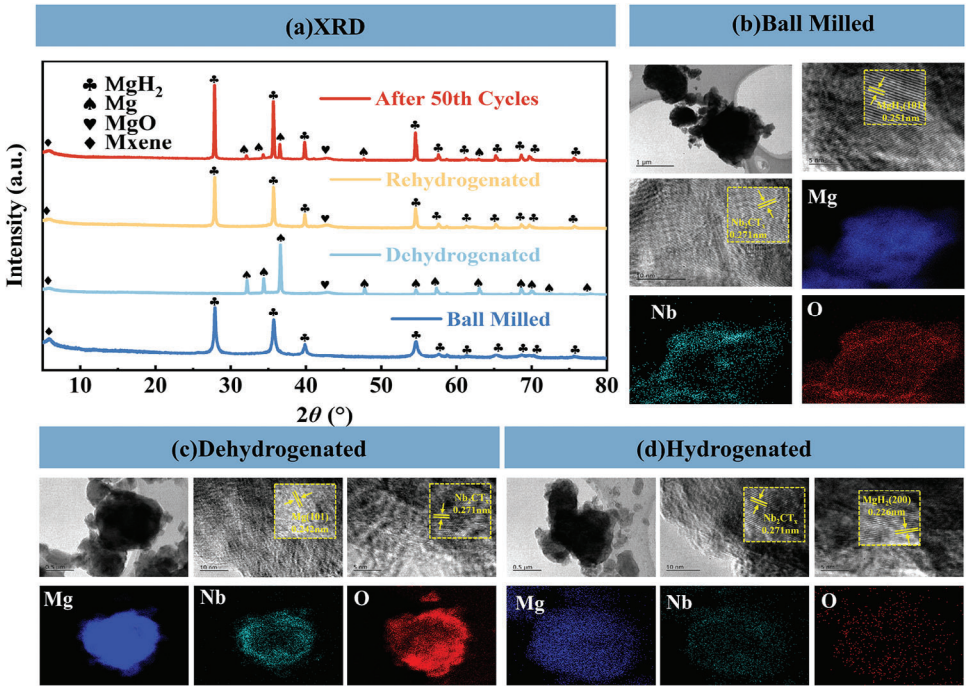

Figure 5. a) XRD spectra of Nb_2CT_x-KOH/MgH_2 composites after ball milling, 1 dehydrogenation cycle, 1 hydrogenation cycle, and 50 hydrogenation cycles at 280 °C; TEM, HRTEM, and elemental mapping images of Nb_2CT_x-KOH/MgH_2 after b) Ball milled, c) Dehydrogenated, and d) Hydrogenated.

Nb_2CT_x-H_2/MgH_2, and Nb_2CT_x- KOH-H_2/MgH_2 dehydrogenation fits show that they are consistently under the penetration model between 235 and 280 °C.

The XRD spectra of Nb_2CT_x-KOH/MgH_2 after the first and 50th hydrogen absorption cycles are shown in **Figure 5a**. It can be seen that Mg is the main phase in the dehydrogenation state, indicating the composite has been completely dehydrogenated at 280 °C. Meanwhile, in the hydrogenated state, small diffraction peaks generated by metal Mg can be identified (Figure 5a). This indicates that a small portion of Mg cannot be hydrogenated during the cycling process, which also explains the reason for the decrease in hydrogen storage capacity after cycling. XRD patterns of Nb_2CT_x-pristine, Nb_2CT_x-H_2, Nb_2CT_x-KOH-Ar, and Nb_2CT_x-KOH-H_2 composites with MgH_2 (Figure S15, Supporting Information) show the same observation. Figure 5b–d shows the TEM and corresponding EDS images of Nb_2CT_x-KOH/MgH_2 composites under ball milling, dehydrogenation, and rehydrogenation conditions. Nb and O elements are distributed uniformly on the surface of the MgH_2 particles as shown by the EDS images. The uniformly distributed catalysts could provide sufficiently stable and catalytically active sites for the dissociation of H_2. In the HRTEM of Nb_2CT_x-KOH/MgH_2, the lattice fringes belonging to Mg/MgH_2 and Nb_2CT_x can be calibrated, which is consistent with the XRD results. The stability of Nb_2CT_x-KOH remains stable during the process of hydrogen uptake and discharge without decomposition or generation of new substances, and the stability of the catalyst contributes to the continued provision of a large number of activation sites and diffusion channels for Mg/MgH_2 during a long cycling process. XPS measurements were used to further understand the changes in surface termination groups during ball milling and cycling. It is worth noting that the percentage of catalyst was increased to 50 wt.% during the XPS characterization process to ensure effective identification of elements. The non-isothermal hydrogen release profile with the addition of 50 wt.% Nb_2CT_x-KOH was comparable to that with the addition of 10 wt.% Nb_2CT_x-KOH (Figure S16, Supporting Information), suggesting a consistent evolution of Nb_2CT_x-KOH in the reaction. Figure S17, (Supporting Information) illustrates the full-region XPS spectra of Nb_2CT_x-KOH/MgH_2 after ball milling and after 50 cycles, showing signals for Mg 1s, Nb 3d, C 1s, and O 1s; no signals were observed for F. Figure S18, (Supporting Information) compared the XPS signals of Mg, Nb, C, and O after ball milling and after 50 cycles. NbC_xO_y $3d_{3/2}$ and NbC_xO_y $3d_{5/2}$ correspond to the surface termination groups (–O and –OH). As shown in Figure S18b, (Supporting Information), the peak intensity of NbC_xO_y in the Nb 3d region did not change after ball milling and cycling. The same conclusion can be drawn from O 1s, where the ratios of –O and –OH remain equal after ball milling. After the prolonged cycling process, the same ratio of –O and –OH peaks can be detected in Figure S18c, (Supporting Information). It is noteworthy that a slight decrease in the peaks belonging to C-Nb-T_x can be observed in Figure S18d, (Supporting Information). This proves that the surface termination groups of Nb_2CT_x are slightly reduced during the long cycling process, which explains the decrease in the kinetics of the cycling process.

To better understand the mechanism of enhancing the hydrogen storage performance, density functional theory (DFT) calculations were utilized to simulate the interaction between hydrogen and Nb_2CT_x (where T represents a defect, oxygen, fluorine, or hydroxide). High-resolution XPS spectra (Figure 2) reveals that four principal functional groups influenced hydrogen storage performance, leading us to construct

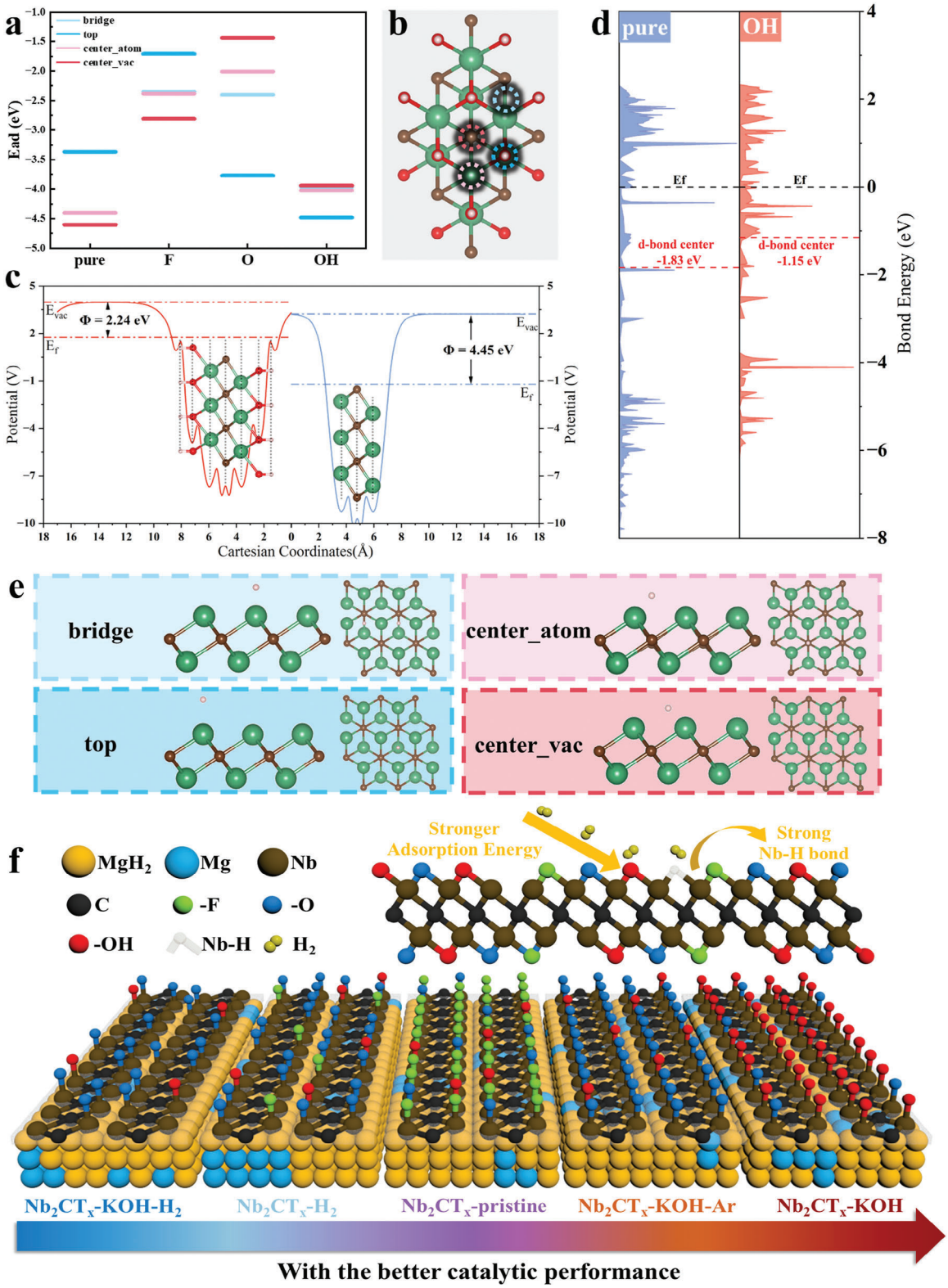

Figure 6. a) Adsorption energy for H atom on virials sites of different matrixes; b) Top view for four different adsorption sites on Nb2C(OH)2; c) Electronic potential distribution along c-axis of Nb2C(OH)2 and Nb2C slab, Φ, Evac and Ef donate work function, vacuum potential, and Fermi energy level respectively; d) PDOS of Nb 4d orbit in Nb2C and Nb2C(OH)2; e) Structure models of four adsorption sites on Nb2C as an example.; f) Mechanism diagram of Nb2CTx catalyzed MgH2 system.

four catalyst models each incorporating a single functional group (designated as pure, –F, –O, and –OH) for targeted analysis. We also accounted for varying adsorption sites on the MXene surface (refer to **Figure 6**b). Figure 6e illustrates these different adsorption scenarios using pure Nb_2C as an example, while Figure 6a compares the adsorption energy across all 16 models. Notably, pure Nb_2C and –OH demonstrated lower adsorption energy compared to F and O. However, experimental data identified –OH as the most beneficial for structure. We found that the most potent adsorption sites varied between the two surfaces. Hydrogen atoms were more attracted to the center of three Nb atoms on the pure surface, rather than on top of hydrogen atoms in the –OH functional group of –OH surface. This suggests different adsorption scenarios – with the hydrogen atom either trapped by a potential well on the pure surface or forming a hydrogen molecule with another hydrogen atom in the –OH group. Additionally, the weak adsorption of –O facilitated hydrogen separation following the formation of H_2 in the –OH group. Work function (Figure 6c) and PDOS (Figure 6d) analyses provide further insight. The –OH model displayed a lower work function, 2.24 versus 4.45 eV for the pure surface, suggesting a greater ease for electrons to escape from the –OH surface to hydrogen, facilitating reduction. The d-bond center, calculated from the PDOS of the Nb 4d orbit, was also closer to the Fermi level in the –OH model, indicating a higher likelihood of d electrons transitioning to the conduction band to catalyze the hydrogen storage reaction. In summary, samples with a higher prevalence of –OH functional groups and fewer defects facilitate faster and easier hydrogen storage and release. The presence of –O functional groups also significantly aids hydrogen release. Experimentally, Nb_2CT_x-KOH most closely aligns with these criteria and demonstrated the best performance, aligning with our calculations. Figure 6f graphically illustrates the catalytic mechanism of the different surface termination groups. Our findings underscore the critical role of surface termination groups in modulating the catalytic performance of MXene-based materials for hydrogen storage, especially on the adsorption energy and work function, offering a promising strategy for the development of efficient hydrogen storage materials.

3. Conclusion

In summary, we have successfully tailored the surface termination groups of Nb_2CT_x MXene by alkali treatment and heat treatment under H_2/Ar to enhance its catalytic activity for MgH_2 hydrogen storage, demonstrating a significant improvement in both dehydrogenation and hydrogenation kinetics. The Nb_2CT_x-KOH-catalyzed MgH_2 composite with optimal surface termination groups reached a remarkable 6.56 wt.% H_2 release in just 5 min at 250 °C and a 6.46 wt.% H_2 uptake within 5 min at 150 °C. Furthermore, the activation energies for dehydrogenation and hydrogen uptake showed substantial reductions of 49.5% and 60.1% compared to pristine MgH_2, respectively. It also achieved a stable de/hydrogenation reaction for at least 50 cycles. A systematic study reveals the introduction of –OH groups or the removal of surface functional groups led to increased adsorption of hydrogen on Nb_2CT_x. Importantly, –OH-enriched Nb_2CT_x exhibited a lower work function (2.24 vs 4.45 eV for the pure surface) and closer d-bond center to the Fermi level, suggesting that the d electrons are more likely to transition to the conduction band to catalyze the hydrogen storage reaction, thus facilitating hydrogen transfer at the interface to enhance the hydrogen adsorption/desorption properties of MgH_2. Our findings underscore the critical role of surface termination groups in modulating the catalytic performance of MXene-based materials for hydrogen storage. The results also highlight the potential of Nb_2CT_x-KOH as a highly effective catalyst for MgH_2 hydrogen storage, offering a promising strategy for the development of efficient hydrogen storage materials.

4. Experimental Section

Materials: Nb_2AlC ceramic powder (≈400 mesh) was purchased from Forsman. HF aqueous solution (50%) was purchased from Macklin Company. Mg powder was purchased from Sinopharm Chemical Reagent Co. 99.99%). MgH_2 was produced by repeated high-temperature hydrogenation and ball milling of Mg powder. The rest of the reagents were provided by Sinopharm Chemical Reagent (Shenzhen) Co.

Synthesis of Nb_2CT_x MXene: The 400 mesh Nb_2AlC powder was stirred in 50% concentrated HF solution for 3 days at room temperature. At the end of the reaction, the suspension was centrifuged and washed several times with deionized water until the pH reached 6. The precipitated powder was harvested by centrifugation and drying in a vacuum.

Modification of Nb_2CT_x MXene: Initially, Nb_2CT_x-pristine (100 mg) was annealed at 500 °C for 30 min in hydrogen to obtain Nb_2CT_x-H_2. Second, Nb_2CT_x-pristine (100 mg) was dispersed in an aqueous KOH solution (5 mL, 10 wt.%) and stirred for 12 h at room temperature. Then it was washed by centrifugation with deionized water several times until pH reached six to obtain Nb_2CT_x-KOH. Nb_2CT_x-KOH was annealed at 500 °C for 30 min in argon/hydrogen to obtain Nb_2CT_x-KOH-Ar/Nb_2CT_x-KOH-H_2.

Preparation of Nb_2CT_x/MgH_2 Composites: The composites were prepared by ball-milling 10 wt.% of five Nb_2CT_x catalysts and MgH_2 for 6 h at a speed of 400 r·min^{-1} with a powder-to-iron ball mass ratio of 1:60. The samples obtained were denoted as Nb_2CT_x-pristine/MgH_2, Nb_2CT_x-H_2/MgH_2, Nb_2CT_x-KOH/MgH_2, Nb_2CT_x-KOH-Ar/MgH_2, Nb_2CT_x-KOH-H_2/MgH_2 respectively. To prevent oxygen and moisture contamination, all operations were conducted in an Ar-filled glove box (Mikrouna) with oxygen/water concentrations kept below 0.1 ppm.

Sample Characterization: The hydrogen ab/desorption experiments were conducted in a Sieverts-type apparatus that was designed and assembled outside of the laboratory. For the non-isothermal decomposition experiments, the samples were heated at a rate of 5 °C min^{-1} from room temperature to 450 °C. For the isothermal dehydrogenation/rehydrogenation experiments, the samples were heated rapidly to the desired temperatures and maintained at a constant pressure of 0.003 MPa/3 MPa hydrogen. The samples' morphology was examined using a scanning electron microscope (SEM, Hitachi SU-70) and a transmission electron microscope (TEM, Tecnai G2 F30, operating voltage 300 kV). X-ray diffractometer (XRD) measurements (Rigaku, 40 kV, and 40 mA) were carried out at a scanning speed of 10° min^{-1} from 20° to 80°. Elemental valence changes of the samples were analyzed by X-ray photoelectron spectroscopy (XPS) using Escalab 250 Xi.

Computational Details: The DFT calculations were carried out using the Vienna ab initio simulation package (VASP) projected augmented wave (PAW) method.[33] The dispersion interactions were described by the van der Waals (vdW) correction DFT-D3, proposed by Grimme, and the exchange-correlation interactions were described by the generalized gradient approximation (GGA) of the Perdew—Burke–Ernzerhof (PBE) function.[34] The plane-wave energy cut-off was set at 550 eV, and all calculations were carried out using a gamma-centered k-point grid with a Kmesh-Resolved value of 0.03 2π Å-1. The structure was relaxed until the forces on all atoms and the total energy converged to less than 0.05 eV Å^{-1} and 1 × 10^{-5} eV. All calculations also took into account the spin

polarization. Monolayer Nb_2C plates with different functional groups were established as simulation models.

Supporting Information

Supporting Information is available from the Wiley Online Library or from the author.

Acknowledgements

T.Z. and T.X. contributed equally to this work. The authors appreciatively acknowledge the financial support from the National Key R&D Program of China (2020YFA0406204).

Conflict of Interest

The authors declare no conflict of interest.

Data Availability Statement

The data that support the findings of this study are available from the corresponding author upon reasonable request.

Keywords

catalytic mechanism, hydrogen storage, magnesium hydride, MXene, surface modulation

Received: September 27, 2024
Revised: October 31, 2024
Published online: November 16, 2024

[1] a) W. Xue, B. Zhao, H. Liu, X. Chen, L. Liu, *Appl. Catal. B-Environ. Energy.* **2024**, *343*, 123574; b) X. Zhang, S. Ju, C. Li, J. Hao, Y. Sun, X. Hu, W. Chen, J. Chen, L. He, G. Xia, F. Fang, D. Sun, X. Yu, *Nat. Commun.* **2024**, *15*, 2815.
[2] A. Schneemann, J. L. White, S. Kang, S. Jeong, L. F. Wan, E. S. Cho, T. W. Heo, D. Prendergast, J. J. Urban, B. C. Wood, M. D. Allendorf, V. Stavila, *Chem. Rev.* **2018**, *118*, 10775.
[3] a) Z. Ma, J. Zang, W. Hu, Q. Wang, Z. Sun, F. Fang, Y. Song, D. Sun, *Adv. Energy Mater.* **2024**, *14*, 2401156; b) C. Zhang, C. Wang, Q. Shi, X. Wang, S. Zhao, L. Liang, Q. Wang, L. Wang, Y. Cheng, *Appl. Catal. B-Environ. Energy.* **2024**, *35*, 124521.
[4] a) Y. Huang, C. An, Y. Liu, Y. Guo, H. Shao, H. Yuan, H. Shao, C. Wang, Y. Wang, *J. Mater. Sci. Technol.* **2025**, *212*, 89; b) C. Li, W. Yang, H. Liu, X. Liu, X. Xing, Z. Gao, S. Dong, H. Li, *Angew. Chem., Int. Ed.* **2024**, *63*, e202320151.
[5] H. Wang, J. Li, X. Wei, Y. Zheng, S. Yang, Y. Lu, Z. Ding, Q. Luo, Q. Li, F. Pan, *Adv. Funct. Mater.* **2024**, *34*, 2406639.
[6] a) Q. Luo, Y. Guo, B. Liu, Y. Feng, J. Zhang, Q. Li, K. Chou, *J. Mater. Sci. Technol.* **2020**, *44*, 171; b) X. Sun, X. Yang, Y. Lu, Q. Luo, C. Wu, Y. Zhang, T. Lyu, Q. Gu, Q. Li, F. Pan, *J. Mater. Sci. Technol.* **2024**, *202*, 119.
[7] a) D. Han, S. Kim, E. Cho, *J. Mater. Chem. A.* **2021**, *9*, 9875; b) Z. Ma, Q. Zhang, S. Panda, W. Zhu, F. Sun, D. Khan, J. Dong, W. Ding, J. Zou, *Sustain. Energy Fuels* **2020**, *4*, 4694.
[8] a) Y. Wang, X. Chen, H. Zhang, G. Xia, D. Sun, X. Yu, *Adv. Mater.* **2020**, *32*, 2002647; b) W. Lin, X. Xiao, X. Wang, J.-W. Wong, Z. Yao, M. Chen, J. Zheng, Z. Hu, L. Chen, *J. Energy Chem.* **2020**, *50*, 296.
[9] a) L. Ren, Y. Li, Z. Li, X. Lin, C. Lu, W. Ding, J. Zou, *Nano-Micro Lett.* **2024**, *16*, 160; b) J. Zhang, W. Wang, X. Chen, J. Jin, X. Yan, J. Huang, *J. Am. Chem. Soc.* **2024**, *146*, 10432; c) C. Duan, Y. Tian, X. Wang, J. Wu, B. Liu, D. Fu, Y. Zhang, W. Lv, L. Hu, F. Wang, X. Zhang, Y. Wu, *Nano Energy* **2023**, *113*, 108536.
[10] a) Y. Yang, X. Zhang, L. Zhang, W. Zhang, H. Liu, Z. Huang, L. Yang, C. Gu, W. Sun, M. Gao, Y. Liu, H. Pan, *J. Mater. Sci. Technol.* **2023**, *163*, 182; b) L. Ren, Y. Li, N. Zhang, Z. Li, X. Lin, W. Zhu, C. Lu, W. Ding, J. Zou, *Nano-Micro Lett.* **2023**, *15*, 93.
[11] Y. Wei, P. Zhang, R. A. Soomro, Q. Zhu, B. Xu, *Adv. Mater.* **2021**, *33*, 2103148.
[12] Z. Du, C. Wu, Y. Chen, Q. Zhu, Y. Cui, H. Wang, Y. Zhang, X. Chen, J. Shang, B. Li, W. Chen, C. Liu, S. Yang, *Adv. Energy Mater.* **2022**, *12*, 2103228.
[13] Q. Gu, Y. Cao, J. Chen, Y. Qi, Z. Zhai, M. Lu, N. Huang, B. Zhang, *Nano-Micro Lett.* **2024**, *16*, 266.
[14] Y. Guo, Q. Zhu, Z. Wang, Y. Ye, J. Hu, J. Shang, B. Li, Z. Du, S. Yang, *Adv. Energy Mater.* **2024**, *14*, 2304149.
[15] a) W. Zhu, L. Ren, C. Lu, H. Xu, F. Sun, Z. Ma, J. Zou, *ACS Nano* **2021**, *15*, 18494; b) Z. Wang, X. Zhang, Z. Ren, Y. Liu, J. Hu, H. Li, M. Gao, H. Pan, Y. Liu, *J. Mater. Chem. A.* **2019**, *7*, 14244; c) H. Liu, X. Duan, Z. Wu, H. Luo, X. Wang, C. Huang, Z. Lan, W. Zhou, J. Guo, M. Ismail, *Chem. Eng. J.* **2023**, *468*, 143688; d) K. Nie, J. Li, H. Lu, R. Zhang, Y. Chen, F. Pan, *Sep. Purif. Technol.* **2025**, *354*, 129069.
[16] M. Li, Q. Huang, *Nat. Mater.* **2024**, *23*, 1017.
[17] J. Zou, J. Wu, Y. Wang, F. Deng, J. Jiang, Y. Zhang, S. Liu, N. Li, H. Zhang, J. Yu, T. Zhai, H. Alshareef, *Chem. Soc. Rev.* **2022**, *51*, 2972.
[18] T. Zhang, L. Chang, X. Zhang, H. Wan, N. Li, L. Zhou, X. Xiao, *Nat. Commun.* **2022**, *13*, 6731.
[19] X. Lv, L. Kou, T. Frauenheim, *ACS Appl. Mater. Interfaces.* **2021**, *13*, 14283.
[20] J. Cai, J. Huang, A. Cao, Y. Wei, H. Wang, X. Li, Z. Jiang, G. I. N. Waterhouse, S. Lu, S. Zang, *Appl. Catal. B-Environ. Energy.* **2023**, *328*, 122473.
[21] C. Huang, S. Shi, H. Yu, *ACS Energy Lett.* **2021**, *6*, 3464.
[22] H. Gao, R. Shi, Y. Liu, Y. Zhu, J. Zhang, L. Li, X. Hu, *J. Magnes. Alloy.* **2023**, *11*, 3724.
[23] Z. Huang, Y. Wang, M. Zhang, *Int. J. Hydrog. Energy.* **2021**, *46*, 33176.
[24] M. Kim, S. Kang, B. Wood, E. Cho, *J. Mater. Chem. A.* **2024**, *12*, 27212.
[25] X. Zhou, H. Guan, H. Lu, Y. Lu, J. Li, J. Wang, Y. Chen, Q. Li, F. Pan, *J. Magnes. Alloy.* https://doi.org/10.1016/j.jma.2023.09.016.
[26] Q. Peng, J. Guo, Q. Zhang, J. Xiang, B. Liu, A. Zhou, R. Liu, Y. Tian, *J. Am. Chem. Soc.* **2014**, *136*, 4113.
[27] J. Luo, X. Tao, J. Zhang, Y. Xia, H. Zhang, Y. Gan, C. Liang, W. Zhang, *ACS Nano* **2016**, *10*, 2491.
[28] S. Tu, F. Ming, J. Zhang, X. Zhang, H. Alshareef, *Adv. Mater.* **2019**, *31*, 1806860.
[29] M. Naguib, J. Halim, J. Lu, K. Cook, L. Hultman, Y. Gogotsi, M. Barsoum, *J. Am. Chem. Soc.* **2013**, *135*, 15966.
[30] E. Xu, H. Li, X. You, C. Bu, L. Zhang, Q. Wang, Z. Zhao, *Int. J. Hydrog. Energy* **2017**, *42*, 8057.
[31] H. Zhou, Z. Chen, E. Kountoupi, A. Tsoukalou, P. M. Abdala, P. Florian, A. Fedorov, C. R. Müller, *Nat. Commun.* **2021**, *12*, 5510.
[32] K. Chou, Q. Li, Q. Lin, L. Jiang, K. Xu, *Int. J. Hydrog. Energy* **2005**, *30*, 301.
[33] a) P. Blochl, *Phys. Rev. B.* **1994**, *50*, 17953; b) G. Kresse, J. Hafner, *Phys. Rev. B.* **1994**, *49*, 14251; c) G. Kresse, J. Furthmüller, *Comp. Mater. Sci.* **1996**, *6*, 15; d) G. Kresse, D. Joubert, *Phys. Rev. B.* **1999**, *59*, 1758.
[34] a) P. John, B. Kieron, E. Matthias, *Phys. Rev. Lett.* **1996**, *77*, 3865; b) S. Grimme, J. Antony, S. Ehrlich, H. Krieg, *J. Chem. Phys.* **2010**, *132*, 154104.